

Goodenough-Kanamori-Anderson rules in 2D magnet: A chemical trend in $M\text{Cl}_2$ with $M=\text{V}$, Mn, and Ni

Thi Phuong Thao Nguyen^{1,2} and Kunihiko Yamauchi^{1,2}

¹*Department of Precision Engineering, Graduate School of Engineering,
Osaka University, 2-1 Yamadaoka, Suita, Osaka 565-0871, Japan*

²*Center for Spintronics Research Network, Osaka University,
1-3 Machikaneyama, Toyonaka, Osaka 560-8531, Japan*

(Dated: August 14, 2023)

Density-functional-theory calculations were performed to investigate the magnetism in a series of triangular-lattice monolayer $M\text{Cl}_2$ ($M=\text{V}$, Mn, and Ni). The magnetic stability manifests a distinct chemical trend; VCl_2 and MnCl_2 show the antiferromagnetic ground states and NiCl_2 shows the ferromagnetic ground state. The microscopic mechanism behind the magnetic interaction is explained by the so-called Goodenough-Kanamori-Anderson rules and by the virtual-hopping process through the hopping integrals between the $3d$ -orbital maximally localized Wannier functions. Our result highlights the role of the direct exchange interaction and the superexchange interaction in the magnetic stabilization in two-dimensional magnets.

I. INTRODUCTION

Recent discoveries of two-dimensional (2D) magnetic van der Waals (vdW) materials have ignited the research boom in exploring further 2D magnetic materials to take advantage of their atomically thin thickness and to examine the novel spintronics applications. [4–6] So far, 2D ferromagnetism has been reported in atomically thin layers of $\text{Cr}_2\text{Ge}_2\text{Te}_3$, CrI_3 and VI_3 in which the transition-metal ion forms a honeycomb structure. [7–11] On the other hand, 2D antiferromagnetism has been reported in NiPS_3 and MnPS_3 , [12, 13]. They are candidate materials for antiferromagnetic (AFM) spintronics applications possibly used in low-energy-consuming and high-speed devices. [14, 15]

In principle, an AFM interaction in the 2D triangular lattice causes magnetic frustration and often results in non-collinear magnetic orderings such as 120° AFM configuration shown in Fig. 1 (e). [16–19] When a strong spin-orbit coupling (SOC) is involved in the system, a *chiral* spin spiral state can be stabilized through an anisotropic magnetic exchange or Dzyaloshinskii-Moriya interaction. It has been reported that monolayer NiI_2 and NiBr_2 show fascinating 2D multiferroic behavior; the ferroelectric polarization is induced by the chiral mag-

netic texture owing to the strong SOC at the heavy halogen atoms. [20–22] While the role of the SOC has been well discussed in previous studies, the basic discussion on magnetic frustration based on the Heisenberg magnetic interactions has not been particularly focused. [23–25]

Along this context, to have a deeper understanding of the AFM interaction and the magnetic frustration in the monolayer triangular lattice, in this work, we investigate a chemical trend of magnetism in monolayer transition-metal dihalides $M\text{Cl}_2$ ($M = \text{V}$, Mn, Ni) in connection with their electronic state. There are two reasons for the choice of these target materials: 1) Since they are composed of light elements, we can ignore the SOC effect and focus on the Heisenberg interactions; 2) in their bulk form, a rich variety of magnetic ground states has been experimentally observed, and it helps us to understand the chemical trend of the magnetism with respect to the different $3d$ electron filling (see Table I). While it has been reported that VCl_2 shows 120° AFM ordering, and NiCl_2 shows FM ordering at low temperatures [3, 26], the magnetic ground state in MnCl_2 is still unclear [2]; recent studies suggested the possibility of its helimagnetic ground state. [27, 28] In the rest of this paper, first, we will discuss the magnetic stability and the exchange coupling in the monolayer halides. Secondly, using the virtual hopping interpretation for magnetic stability, we will discuss the microscopic mechanism behind the magnetic interaction.

II. METHODOLOGY

Transition-metal dihalides MX_2 form a triangular lattice in which the cation M is surrounded by six ligand X anions in octahedron coordination, as illustrated in Fig. 1 (a). In the bulk form, VCl_2 crystallize in the trigonal CdI_2 structure ($P\bar{3}m1$ space group) and MnCl_2 and NiCl_2 crystallize in the rhombohedral CdCl_2 structure ($R\bar{3}m$ space group). These two structure types have

Bulk (experiment)			
	T_C	Magnetic order	In-plane order
VCl_2 [1]	35.8	ncl	120° -AFM
MnCl_2 [2]	2.0, 1.8	unclear	unclear
NiCl_2 [3]	52	col	FM

TABLE I. Summary of experimentally reported magnetic property for bulk $M\text{Cl}_2$ compounds. T_C (K) is the ordering temperature of collinear (col) or noncollinear (ncl) AFM and FM orderings. In-plane order shows the arrangement of the magnetic moments in a single atomic layer.

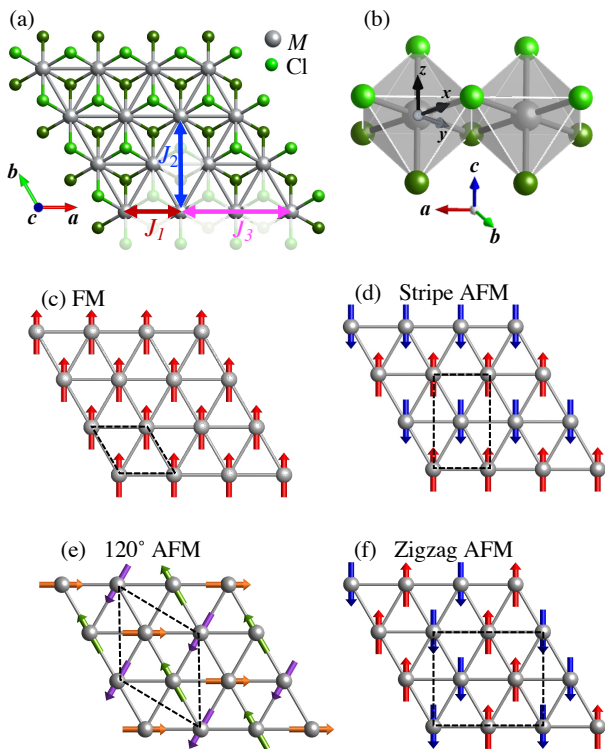


FIG. 1. (a) Crystal structure of monolayer $M\text{Cl}_2$ in a triangular lattice (corresponding to 1T phase in bulk). Dark and light green balls represent Cl atoms in the lower and upper layers, respectively, while grey balls represent M atoms. The double-headed arrow indicates the in-plane exchange coupling J_{ij} . (b) Neighboring $M\text{Cl}_6$ octahedra sharing the edge. The local coordinate system $\{xyz\}$ in an octahedron and the hexagonal lattice vectors $\{abc\}$ are shown by black and colorful arrows, respectively. (c-f) Magnetic configurations considered in this study. The black dashed line indicates the magnetic supercells used in the calculations.

different stackings along the c -axis, whereas they have the same in-plane atomic structure. Individual layers of dihalides can be extracted from the bulk using exfoliation techniques. To calculate the electronic state in the monolayer $M\text{Cl}_2$, we set up the slab model containing one monolayer and 18 \AA length of vacuum region in a periodic supercell.

Density-functional theory (DFT) calculations were performed using VASP [29, 30] code with generalized gradient approximation (GGA) [31]. Hubbard U potential, $U = 1.8 \text{ eV}$ and $J_{\text{H}} = 0.8 \text{ eV}$ for V, Mn, and Ni $3d$ orbital state, was employed within the Liechtenstein approach. [24, 32] The atomic positions and the lattice parameters were optimized in FM configuration until forces acting on atoms were smaller than 0.1 eV/\AA (the results are shown in Table. II). To evaluate the magnetic stability and to extract the Heisenberg exchange coupling constants, J_{ij} , we considered four different spin order arrangements, that is, ferromagnetic (FM), stripe-type AFM, 120° frustrated AFM, and zigzag-type AFM configurations, shown in Fig. 1 (c-f). The minimum size of

supercells was used for each AFM configuration — containing two, three, and four f.u. for stripe AFM, 120° AFM, and zigzag AFM configurations, respectively — to reduce the computational cost. While the k -point mesh was set to be $18 \times 18 \times 1$ for the unit cell, we used $18 \times 10 \times 1$, $10 \times 10 \times 1$, and $10 \times 9 \times 1$, for these AFM supercells, respectively. The difference of total energy, $\Delta E = E_{\text{AFM}} - E_{\text{FM}}$, was calculated between AFM and FM configurations in the same supercell and with the same k -point mesh. By taking the difference, we can eliminate the energy terms that depend on the supercell shape and extract the energy purely related to the magnetic stability.

After the self-consistent calculation in FM configuration converged, the Bloch functions relevant to five M - d bands and six Cl- p bands (for each spin state) were projected onto the maximally localized Wannier functions (MLWFs) by using the Wannier90 tool to evaluate the hopping parameters between the M - $3d$ orbital states. [33–35] The obtained hopping parameter t implicitly contains both the direct $d-d$ hopping and the indirect $d-p-d$ hopping processes since the Wannier functions have delocalized character reflecting the hybridization between M - $3d$ orbital states and ligand Cl- p orbital states.

III. RESULTS AND DISCUSSIONS

A. Electronic state and crystal-field splitting

Figure 2 shows the calculated density of states (DOS). Since the octahedral crystalline electric field splits the d orbital states into the two-fold e_g and three-fold t_{2g} states, all the materials show the insulating state with the band gap, 2.0 eV , 2.36 eV and 1.66 eV for VCl_2 , MnCl_2 and NiCl_2 , respectively, which is in agreement with previous studies. [16, 24, 36] In VCl_2 , the V^{2+} (d^3) ion exhibits the high-spin ($S = 3/2$) state with the empty e_g^\uparrow and occupied t_{2g}^\uparrow states in the majority spin state. There is no significant splitting between e_g^\downarrow and t_{2g}^\downarrow states in the minority spin state due to the weak hybridization of the d^\downarrow states in higher energy with the Cl- p states located below the Fermi energy. In MnCl_2 , the Mn^{2+} (d^5) ion exhibits the high-spin ($S = 5/2$) state with the fully occupied (unoccupied) majority-spin (minority-spin) state. In NiCl_2 the Ni^{2+} (d^8) ion exhibits the high-spin ($S = 1$) state with the fully occupied majority-spin state and the occupied t_{2g}^\downarrow state and the empty e_g^\downarrow state in the minority-spin channel.

B. Magnetic stability and exchange interaction

The transition-metal spin momenta were calculated as $2.63 \mu_{\text{B}}$, $4.51 \mu_{\text{B}}$ and $1.51 \mu_{\text{B}}$ for VCl_2 , MnCl_2 and NiCl_2 , respectively, comparable to their nominal spin

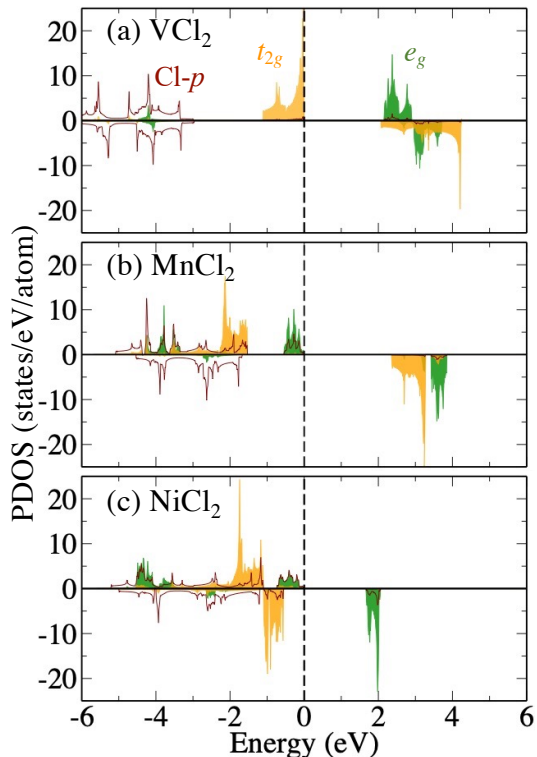


FIG. 2. DOS projected onto transition-metal 3d and Cl-2p state with O_h crystal-field states via MLWFs. Green (orange) filled-curve represents e_g (t_{2g}) states. The brick red curve represents for p state. Fermi level is set at energy origin.

	a	θ	M -Cl	NN ^{1st}	NN ^{2nd}	NN ^{3rd}
VCl ₂	3.54	91.07°	2.48	3.54	6.13	7.08
MnCl ₂	3.70	93.16°	2.55	3.70	6.41	7.40
NiCl ₂	3.49	93.27°	2.40	3.49	6.04	6.98

TABLE II. Optimized structural parameters: in-plane lattice constant a (Å); M -Cl- M angle θ (°), M -Cl bond lengths (Å); distance (Å) between first (NN^{1st}), second (NN^{2nd}), and third (NN^{3rd}) nearest neighbor transition-metal-ionic sites.

sizes, $S = 3, 5, 2 \mu_B$, respectively. Table III shows the evaluated magnetic stability for the monolayers. VCl₂ strongly favors 120° AFM spin configuration, being consistent with a neutron diffraction study for bulk VCl₂ reporting the in-plane 120° AFM spin configuration (see also Table I).[1] In MnCl₂, although 120° AFM order is slightly preferred, three AFM spin configurations are very close in the energy. A neutron diffraction study reported that there are two magnetic phase transitions at $T_N = 1.81$ and 1.96 K, but the spin configuration at the ground state has not been clarified.[2] Making a keen contrast, NiCl₂ shows a strong preference for FM ordering. This is consistent with previous experimental findings of the in-plane FM configuration with out-of-plane AFM ordering. [3, 37, 38]

To understand the magnetic stability, we evaluated the

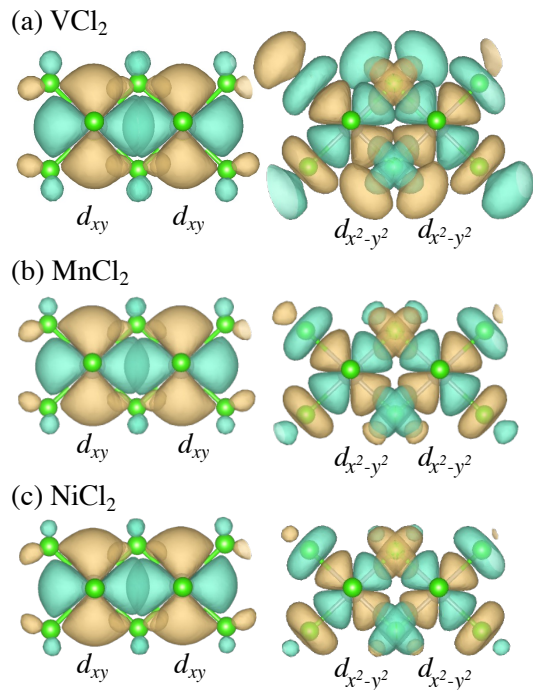


FIG. 3. The MLWFs relevant to the two dominant nearest-neighbor hoppings between d_{xy} and d_{xy} , and between $d_{x^2-y^2}$ and $d_{x^2-y^2}$ orbitals. Isosurface level was set at $\pm 0.2 a_0^{-3/2}$, where a_0 is the Bohr radius.

magnetic exchange interactions (J_{ij}) between M atoms by fitting the total energy differences to the Heisenberg Hamiltonian:

$$H = \sum_{\langle ij \rangle} J_{ij} s_i \cdot s_j \quad (1)$$

where s_i and s_j are the spin unit vectors at the site i and site j . When $J < 0$ ($J > 0$), a parallel spin (anti-parallel spin) configuration is preferred. In the triangular lattice monolayer, we consider J_1 , J_2 , and J_3 exchange couplings, corresponding to the first, second, and third nearest neighbor interactions, as illustrated in Fig. 1 (a). In order to derive these parameters, the total energy of four magnetic configurations in Fig. 1 are mapped onto the Heisenberg Hamiltonian. Equation 1 for the AFM configurations can be written as

$$\begin{aligned} E_{\text{stripe}} &= -2J_1 - 2J_2 + 6J_3, \\ E_{120^\circ} &= -9/2J_1 + 9J_2 - 9/2J_3, \\ E_{\text{zigzag}} &= -4J_1 + 4J_2 - 4J_3, \end{aligned} \quad (2)$$

per each magnetic supercell. Then we calculated the difference between AFM and FM total energy as $\Delta E = E_{\text{AFM}} - E_{\text{FM}}$ for each magnetic supercell and solved the simultaneous equations for J_1 , J_2 , and J_3 . The FM total energy is defined as $E_{\text{FM}} = 3n(J_1 + J_2 + J_3)$ where $n = 2, 3, 4$ denotes the size of the magnetic supercell.

The ferromagnetic and antiferromagnetic transition temperatures (T_C and T_N) were evaluated within the

ΔE	Stripe	120°	Zigzag	FM
VCl ₂	-78.41	-85.53	-75.07	0.00
MnCl ₂	-8.82	-10.23	-9.94	0.00
NiCl ₂	+19.82	+17.57	+13.09	0.00
J_{ij}	J_1	J_2	J_3	T_C, T_N
VCl ₂	+20.08	-0.48	-1.07	115.8
MnCl ₂	+1.78	+0.43	+0.49	8.3
NiCl ₂	-6.22	+1.26	+2.31	30.7

TABLE III. Top: Calculated total energy ΔE (meV/f.u) for each magnetic configuration with respect to FM configuration; the lowest energy is highlighted. Bottom: Exchange coupling constants J_1, J_2, J_3 (meV) and the critical temperature T_C and T_N (K).

mean-field approximation [39, 40] as follows:

$$T_C = -1/3k_B(3J_1 + 3J_2 + 3J_3), \quad (3)$$

$$T_N = -1/3k_B(-3/2J_1 + 3J_2 - 3/2J_3), \quad (4)$$

where k_B is the Boltzmann constant.

The calculated magnetic exchange coupling constants are tabulated in Table III. The first nearest interaction J_1 is the dominant interaction that leads to the 120°-AFM ground state in VCl₂ and MnCl₂, and FM ground state in NiCl₂. While the estimated critical temperatures are overestimated owing to the mean-field approximation, we can still qualitatively discuss the magnetic stability along the chemical trend. In MnCl₂, J_1, J_2 , and J_3 show all small positive values and lead to the competing stability between several AFM configurations. This may be responsible for the theoretically predicted spin-spiral ground state.[27] For all three chlorides, the longer-range interaction J_2 is much smaller than J_1 , while J_3 is found to be larger than J_2 . This trend ($|J_1| \gg |J_3| > |J_2|$) is consistent with a previous theoretical work [24] and characteristic of the triangular lattice; the edge-sharing MCl_6 octahedral geometry allows both direct ($d-d$ or $d-d-d$) hoppings and indirect ($d-p-d$ or $d-p-d-p-d$) hoppings in J_1 and J_3 interactions while only the indirect ($d-p-d-p-d$) hopping is possible for J_2 interaction.

To understand the J_1 character for these chlorides, we apply the Goodenough-Kanamori-Anderson (GKA) rules that commonly explain the magnetic interaction in transition-metal oxides to the superexchange interaction in the 90° angle $M-Cl-M$ bond. According to the GKA rule, —the third rule made for 90° bonds—, 1) $e_g - e_g$ exchange is ferromagnetic and weak, 2) direct $t_{2g} - t_{2g}$ interaction can be antiferromagnetic and 3) indirect $t_{2g} - p - t_{2g}$ and $t_{2g} - p - e_g$ interactions can be either strong antiferromagnetic or (weak) ferromagnetic dependent on the orbital occupation. [41–44] Therefore, we can deduce a consistent conclusion. For VCl₂, $t_{2g}^{3\uparrow} - p - t_{2g}^{0\downarrow}$ exchange may result in the AFM interaction. For MnCl₂, $e_g^{2\uparrow} - p - t_{2g}^{0\downarrow}$ exchange may cause FM interaction, but also $t_{2g}^{3\uparrow} - p - t_{2g}^{0\downarrow}$ exchange may counteract, and thus the net interaction may become weak. For NiCl₂, $e_g^{2\uparrow} - p - t_{2g}^{0\downarrow}$

VCl ₂	d_{xy}	d_{yz}	d_{zx}	$d_{x^2-y^2}$	d_{z^2}
d_{xy}	-250	12	13	4	-33
d_{yz}	12	68	-38	-12	-2
d_{zx}	13	-38	72	11	-2
$d_{x^2-y^2}$	4	-12	11	-162	2
d_{z^2}	-33	-2	-2	2	-7

MnCl ₂	d_{xy}	d_{yz}	d_{zx}	$d_{x^2-y^2}$	d_{z^2}
d_{xy}	-81	7	7	1	0
d_{yz}	7	20	-9	-7	-1
d_{zx}	7	-9	21	6	-1
$d_{x^2-y^2}$	1	-7	6	-67	0
d_{z^2}	0	-1	-1	0	7

NiCl ₂	d_{xy}	d_{yz}	d_{zx}	$d_{x^2-y^2}$	d_{z^2}
d_{xy}	-77	7	7	0	4
d_{yz}	7	20	-9	-7	0
d_{zx}	7	-9	21	6	0
$d_{x^2-y^2}$	0	-7	6	-69	0
d_{z^2}	4	0	0	0	13

TABLE IV. Hopping integrals t_{dd} (meV) calculated by MLWF basis set of the nearest-neighbor $M-d$ orbital states. The dominant elements are highlighted.

may result in FM interaction. This is also consistent with a discussion made by Kanamori on 90° superexchange interactions between V^{2+} sites ($d^3 - d^3$) and Ni^{2+} sites ($d^8 - d^8$) concluding, resulting in AFM and FM couplings, respectively. [42]

In the current study, we will take a step further by presenting a quantitative analysis of the $d-d$ hopping integrals. In Mott insulators, the direct exchange coupling is approximated as $J \sim \sum_{m,n} 2t_{mn}^2 / \Delta E_{mn}$ with $d-d$ hopping integral t_{mn} between occupied m and unoccupied n orbital states at neighboring transition-metal sites and the difference of those energy levels ΔE_{mn} (in the case of two orbital state model, it corresponds to on-site Coulomb repulsion U that separates the filled and the unfilled energy levels); this process is known as “*virtual hopping*” [44]. If the hopping is stronger between orbital states that belong to the same spin states than that for opposite spin states, it leads to a parallel-spin configuration; on the other hand, if hopping between orbitals that belong to the opposite spin states is stronger, it leads to the anti-parallel spin configuration. Hereinafter, we assume that the hopping integral is not significantly modified by a change in the spin configurations and in the energy level, and therefore, we evaluate the orbital dependency of the hopping integral calculated in FM state.

The calculated $d-d$ hopping integrals t_{dd} between the first nearest neighbor M atomic sites are shown in Table IV. A common feature among those chlorides is found that $t_{xy,xy}$ and $t_{x^2-y^2,x^2-y^2}$ dominate over the $d-d$

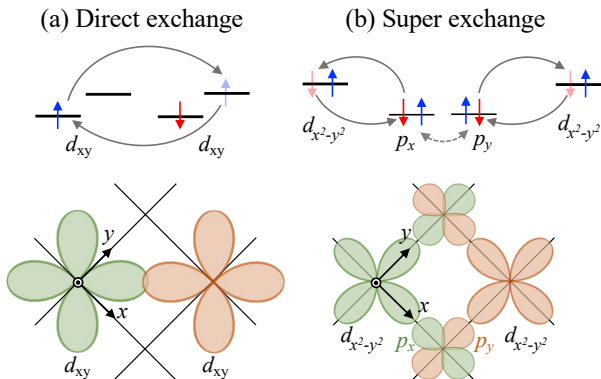


FIG. 4. Schematic pictures of (a) direct exchange and (b) superexchange interactions between the nearest-neighbor M - $3d$ orbitals. Direct exchange stabilizes an anti-parallel spin configuration due to the virtual hopping process. Super exchange stabilizes a parallel spin configuration due to the virtual hopping process together with the Hund's coupling at Cl site.

hopping integrals. As is typical in the edge-sharing octahedra, neighboring d_{xy} orbitals can directly interact through the orbital lobes pointing toward each other, resulting in the largest hopping integral. On the other hand, $t_{x^2-y^2, x^2-y^2}$ shows rather indirect hopping characteristic. The tails of the neighboring Wannier functions show a large overlap in the vicinity of Cl sites. This leads to $d-p-p-d$ superexchange interaction. Both $t_{xy, xy}$ and $t_{x^2-y^2, x^2-y^2}$ hopping integrals manifest an obvious chemical trend — they decrease from V to Mn to Ni. This is explained by the incomplete screening of core potential. [45] When one electron and one proton are added to an atom, the electron incompletely screens the attractive potential from the proton seen by another valence electron. It makes the one-electron potential become deeper and deeper as the valence electrons increase. Therefore, Ni- d orbital state is more localized than V- d orbital state, and the hopping is suppressed (compare the spreading of the Wannier functions in Fig. 3).

The direct $d_{xy} - d_{xy}$ hopping leads to an anti-parallel spin configuration by the direct exchange process if the electron occupying the majority-spin state can hop to the empty minority-spin state in a neighboring atom (see Fig. 4 (a)). This causes anti-parallel-spin coupling in VI_2 where d_{xy} state is occupied only in one spin channel. On the other hand, the indirect $t_{x^2-y^2, x^2-y^2}$ hopping leads to

a parallel spin configuration by the superexchange process mediated by the Cl- p Hund's coupling that favors parallel spin configuration at Cl site if Cl- p electron can hop onto the partially unoccupied $d_{x^2-y^2}$ orbital state (see Fig. 4 (b)). This causes parallel-spin coupling in NiCl_2 , where $d_{x^2-y^2}$ state is occupied only in one spin channel. In MnCl_2 , both the direct and the superexchange processes are possible to take place; their competition ends up with its weak magnetic interaction.

IV. CONCLUSIONS

By means of density-functional-theory calculations, we investigated the magnetism in monolayer $M\text{Cl}_2$. Our result shows good agreement with the experimental reports; VCl_2 favors the AFM configuration, NiCl_2 favors the FM configuration, and MnCl_2 shows the weak magnetic interaction. Considering the chemical trend, we confirmed that the Goodenough-Kanamori-Anderson rules still stand in the monolayer transition-metal chlorides. On top of it, it should be emphasized that d_{xy} and $d_{x^2-y^2}$ orbital states play an important role to determine the exchange interaction in the 2D magnets. This finding may provide insights into the magnetism, typically associated with the frustrated magnetism such as helimagnetism and skyrmion in recently developed 2D materials.

ACKNOWLEDGMENTS

This work was supported by JST-CREST (Grant No. JPMJCR18T1). The computation in this work has been done using the facilities of the Supercomputer Center, the Institute for Solid State Physics, the University of Tokyo and Supercomputing System MASAMUNE-IMR in the Center for Computational Materials Science, Institute for Materials Research, Tohoku University (Project No. 20K0045). The crystallographic figure was generated using the VESTA program [46].

Appendix: Electronic band structure

Figure A-1 shows the calculated bandstructure of monolayer NiCl_2 fitted by the MLWF bands.

- [1] H. Kadowaki, K. Ubukoshi, K. Hirakawa, J. L. Martínez, and G. Shirane, *J. Phys. Soc. Jpn.* **56**, 4027 (1987).
- [2] R. B. Murray, *Phys. Rev.* **128**, 1570 (1962).
- [3] A. Ferrari, A. Braibanti, and G. Bigliardi, *Acta Cryst.* **16**, 846 (1963).
- [4] M. Gibertini, M. Koperski, A. F. Morpurgo, and K. S. Novoselov, *Nat. Nanotechnol.* **14**, 408 (2019).

- [5] Q. H. Wang, A. Bedoya-Pinto, M. Blei, A. H. Dismukes, A. Hamo, S. Jenkins, M. Koperski, Y. Liu, Q.-C. Sun, E. J. Telford, H. H. Kim, M. Augustin, U. Vool, J.-X. Yin, L. H. Li, A. Falin, C. R. Dean, F. Casanova, R. F. L. Evans, M. Chshiev, A. Mishchenko, C. Petrovic, R. He, L. Zhao, A. W. Tsen, B. D. Gerardot, M. Brotons-Gisbert, Z. Guguchia, X. Roy, S. Tongay, Z. Wang, M. Z. Hasan, J. Wrachtrup, A. Yacoby, A. Fert, S. Parkin, K. S.

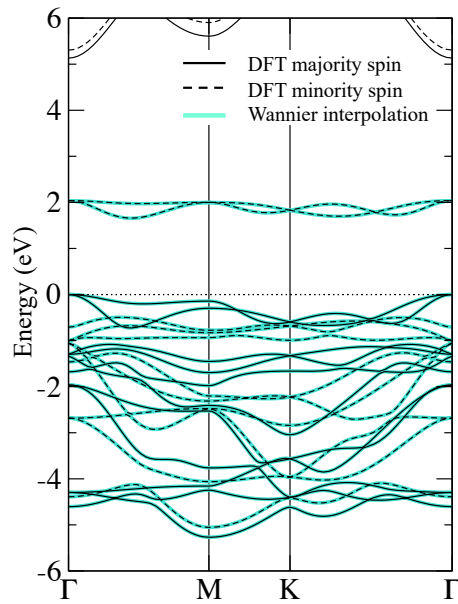


FIG. A-1. Energy bandstructure obtained from the DFT calculations (black solid and dashed lines) and from the MLWF interpolation (cyan lines) of monolayer NiCl_2 along the high-symmetry lines. The Fermi energy is set at zero.

- Novoselov, P. Dai, L. Balicas, and E. J. G. Santos, *ACS Nano* **16**, 6960 (2022).
- [6] M. A. McGuire, *Crystals* **7**, 121 (2017).
- [7] C. Gong, L. Li, Z. Li, H. Ji, A. Stern, Y. Xia, T. Cao, W. Bao, C. Wang, Y. Wang, Z. Q. Qiu, R. J. Cava, S. G. Louie, J. Xia, and X. Zhang, *Nature* **546**, 265 (2017).
- [8] B. Huang, G. Clark, E. Navarro-Moratalla, D. R. Klein, R. Cheng, K. L. Seyler, D. Zhong, E. Schmidgall, M. A. McGuire, D. H. Cobden, W. Yao, D. Xiao, P. Jarillo-Herrero, and X. Xu, *Nature* **546**, 270 (2017).
- [9] S. Jiang, L. Li, Z. Wang, K. F. Mak, and J. Shan, *Nat. Nanotechnol.* **13**, 549 (2018).
- [10] S. Son, M. J. Coak, N. Lee, J. Kim, T. Y. Kim, H. Hamidov, H. Cho, C. Liu, D. M. Jarvis, P. A. C. Brown, J. H. Kim, C.-H. Park, D. I. Khomskii, S. S. Saxena, and J.-G. Park, *Phys. Rev. B* **99**, 041402(R) (2019).
- [11] T. P. T. Nguyen, K. Yamauchi, T. Oguchi, D. Amoroso, and S. Picozzi, *Phys. Rev. B* **104**, 014414 (2021).
- [12] K. Kim, S. Y. Lim, J.-U. Lee, S. Lee, T. Y. Kim, K. Park, G. S. Jeon, C.-H. Park, J.-G. Park, and H. Cheong, *Nat. Commun.* **10**, 345 (2019).
- [13] K. Kim, S. Y. Lim, J. Kim, J.-U. Lee, S. Lee, P. Kim, K. Park, S. Son, C.-H. Park, J.-G. Park, and H. Cheong, *2D Materials* **6**, 041001 (2019).
- [14] V. Baltz, A. Manchon, M. Tsoi, T. Moriyama, T. Ono, and Y. Tserkovnyak, *Rev. Mod. Phys.* **90**, 015005 (2018).
- [15] S. Rahman, J. F. Torres, A. R. Khan, and Y. Lu, *ACS Nano* **15**, 17175 (2021).
- [16] V. V. Kulish and W. Huang, *J. Mater. Chem. C* **5**, 8734 (2017).
- [17] J. Luo, G. Xiang, Y. Tang, K. Ou, and X. Chen, *J. Appl. Phys.* **128**, 113901 (2020).
- [18] Y. Yekta, H. Hadipour, E. Şaşıoğlu, C. Friedrich, S. A. Jafari, S. Blügel, and I. Mertig, *Phys. Rev. Materials* **5**, 034001 (2021).
- [19] B. Zhang, X. Chen, F. Deng, X. Lv, C. Zhang, B. Zheng, H. Wang, and J. Wang, *Appl. Phys. Lett.* **121** (2022).
- [20] D. Amoroso, P. Barone, and S. Picozzi, *Nat. Commun.* **11**, 5784 (2020).
- [21] Q. Song, C. A. Occhialini, E. Ergeçen, B. Ilyas, D. Amoroso, P. Barone, J. Kapeghian, K. Watanabe, T. Taniguchi, A. S. Botana, S. Picozzi, N. Gedik, and R. Comin, *Nature* **602**, 601 (2022).
- [22] A. O. Fumega and J. L. Lado, *2D Materials* **9**, 025010 (2022).
- [23] T. B. Prayitno and F. Ishii, *J. Phys. Soc. Jpn.* **88**, 104705 (2019).
- [24] K. Riedl, D. Amoroso, S. Backes, A. Razpopov, T. P. T. Nguyen, K. Yamauchi, P. Barone, S. M. Winter, S. Picozzi, and R. Valentí, *Phys. Rev. B* **106**, 035156 (2022).
- [25] M.-C. Wang and C.-R. Chang, *J. Am. Chem. Soc.* **169**, 053507 (2022).
- [26] H. Kadowaki, K. Ubukoshi, K. Hirakawa, J. L. Martínez, and G. Shirane, *J. Phys. Soc. Jpn.* **56**, 4027 (1987).
- [27] T. B. Prayitno and F. Ishii, *J. Phys. Soc. Jpn.* **88**, 104705 (2019).
- [28] D. G. Wiesler, M. Suzuki, I. S. Suzuki, and N. Rosov, *Phys. Rev. B* **55**, 6382 (1997).
- [29] G. Kresse and J. Furthmüller, *Phys. Rev. B* **54**, 11169 (1996).
- [30] P. E. Blöchl, *Phys. Rev. B* **50**, 17953 (1994).
- [31] J. P. Perdew, K. Burke, and M. Ernzerhof, *Phys. Rev. Lett.* **77**, 3865 (1996).
- [32] A. I. Liechtenstein, V. I. Anisimov, and J. Zaanen, *Phys. Rev. B* **52**, R5467 (1995).
- [33] A. A. Mostofi, J. R. Yates, Y.-S. Lee, I. Souza, D. Vanderbilt, and N. Marzari, *Comput. Phys. Commun.* **178**, 685 (2008).
- [34] N. Marzari, A. A. Mostofi, J. R. Yates, I. Souza, and D. Vanderbilt, *Rev. Mod. Phys.* **84**, 1419 (2012).
- [35] G. Pizzi, V. Vitale, R. Arita, S. Blügel, F. Freimuth, G. Géranton, M. Gibertini, D. Gresch, C. Johnson, T. Koretsune, J. Ibañez-Azpiroz, H. Lee, J.-M. Lihm, D. Marchand, A. Marrazzo, Y. Mokrousov, J. I. Mustafa, Y. Nohara, Y. Nomura, L. Paulatto, S. Poncé, T. Ponweiser, J. Qiao, F. Thöle, S. S. Tsirkin, M. Wierzbowska, N. Marzari, D. Vanderbilt, I. Souza, A. A. Mostofi, and J. R. Yates, *J. Phys. Condens. Matter* **32**, 165902 (2020).
- [36] A. S. Botana and M. R. Norman, *Phys. Rev. Materials* **3**, 044001 (2019).
- [37] R. H. Busey and W. F. Giaque, *J. Am. Chem. Soc.* **74**, 4443 (1952).
- [38] K. Katsumata and K. Yamasaka, *J. Phys. Soc. Jpn.* **34**, 346 (1973).
- [39] A. Liechtenstein, M. Katsnelson, V. Antropov, and V. Gubanov, *J. Magn. Magn. Mater.* **67**, 65 (1987).
- [40] D. Okuyama, K. Yamauchi, H. Sakai, Y. Taguchi, Y. Tokura, K. Sugimoto, T. J. Sato, and T. Oguchi, *Phys. Rev. Res.* **2**, 033038 (2020).
- [41] J. B. Goodenough, *Phys. Rev.* **100**, 564 (1955).
- [42] J. Kanamori, *J. Phys. Chem. Solids* **10**, 87 (1959).
- [43] P. W. Anderson, *Phys. Rev.* **79**, 350 (1950).
- [44] D. I. Khomskii, *Transition Metal Compounds* (Cambridge University Press, 2014).
- [45] M. W. Haverkort, M. Zwierzycki, and O. K. Andersen, *Phys. Rev. B* **85**, 165113 (2012).
- [46] K. Momma and F. Izumi, *J. Appl. Cryst.* **44**, 1272 (2011).